Design Optimization of Origami-Tunable Frequency Selective Surfaces

KAZUKO FUCHI[1,2], DEANNA SESSIONS [3], ANDREW GILLMAN [4] (Member, IEEE),
VENKATESH MEENAKSHISUNDARAM[4,5], ALEXANDER COOK[4,5],
GREGORY H. HUFF [3] (Senior Member, IEEE), AND PHILIP R. BUSKOHL [4]

[1]Applied Mechanics Division, University of Dayton Research Institute, Dayton, OH 45469, USA

[2]Aerospace Systems Directorate, Air Force Research Laboratory, Wright-Patterson AFB, OH 45433, USA

[3]Department of Electrical Engineering, Pennsylvania State University, University Park, PA 16801, USA

[4]Materials and Manufacturing Directorate, Air Force Research Laboratory, Wright-Patterson AFB, OH 45433, USA

[5]UES Inc., Beavercreek, OH 45432, USA

CORRESPONDING AUTHOR: P. R. BUSKOHL (e-mail: philip.buskohl.1@us.af.mil)

ABSTRACT Recent studies demonstrate the benefit of integrating origami in many engineering applications, where computational methods facilitate the origami design process. An emerging concept utilizes origami design for physically and functionally flexible electromagnetic devices. However, coupled mechanical and electromagnetic design tools are needed to systematically navigate the complex spaces of fold topology and electromagnetic performance. In this article, we introduce topology optimization formulations that find origami fold-driven frequency selective surface designs possessing electromagnetic filtering properties at target frequencies. These formulations utilize a nonlinear mechanics analysis to simulate an origami folding process. A geometric mapping relates mechanically-relevant origami substrate properties and electromagnetically-relevant conductive element properties. Both gradient-based and genetic algorithm methods are used to find optimal origami crease patterns and folded configurations by optimizing fold stiffness and force distributions over a prescribed potential fold line network. Using nonlinear manifold learning techniques, we demonstrate the isolated nature of optimal design candidates in the design space and the complex interplay of fold topology and fold path selection through initial perturbation from the flat state. Collectively, this study provides an initial framework to design novel EM origami structures and also provides important insights on the complex nature of the design space, which can be leveraged to refine future tool development.

INDEX TERMS Topology, frequency selective surfaces, unsupervised learning, structural shapes, periodic structures.

I. INTRODUCTION

ORIGAMI, the art of paper folding, offers a large variety of engineering applications such as satellite or antenna deployment [1]–[4], self-folding micro-devices and robots [5], [6], tunable stiffness structures [7], acoustic energy focusing [8]–[11] and frequency tuning and reconfiguration in electromagnetic devices [12]–[18]. Integrating this intricate art form in engineering design provides the advantage of transforming a 2D manufacturing process into a 3D functional space with many degrees of freedom. Lang had conceptualized connecting the art of origami, mathematics and computer technology in the 1990's and demonstrated a computational method assisting origami design in his TreeMaker [19], which computes a crease pattern for a given stick figure (tree) that traces the desired origami base.

Today, many of the most complex and exquisite origami models are designed with the aid of a computational method. A systematic method for designing an origami structure with multi-functional outcomes continues to be important challenge for the full integration of origami in technology.

Mechanical Variables		Electromagnetic Variables	
α	Fold stiffness design variable	$\vec{E}$	Electric field vector
β	Out-of-plane loading design variable	ϵ_r	Relative permittivity
E	Young's modulus	μ_r	Relative permeability
ϵ	Axial strain	$\boldsymbol{k}$	Wave vector
$\boldsymbol{X_n}$	Substrate coordinate	f^*	Operating frequency
$\boldsymbol{u_i}$	Displacement vector	w	Dipole width
$\boldsymbol{F_i}$	External force	l_d	Dipole length
G	Torsional spring constant	$\boldsymbol{p_i}$	Dipole coordinates

Tachi's Origamizer [20] computes a crease pattern that reproduces a target 3D geometry through origami, addressing how to make a specified 3D form with rigid facets. Pereza-Hernandez *et al.* [21] offers a method to achieve a specified 3D form through the use of smooth folds. Other approaches include a flat foldable 3D polygon design method by Kase *et al.* [22], a flat foldable quadrilateral mesh design method by Feng *et al.* [23], a prism synthesis method by Abdul-Sater [24], and an inverse design method for deployable origami structures by Dang *et al.* [25]. In this study, we develop a design optimization framework to capture both mechanical and electromagnetic (EM) functionality from the robust reconfiguration capability of origami.

Integrating origami design in EM devices has significant practical implications in frequency tuning [13], [17], [26]–[29] and antenna reconfiguration and deployment [3], [4], [12], [18], [30]–[32]. The merit of a systematic origami design method is emphasized in such areas because it provides an efficient exploration method for previously overlooked design spaces. In addition, physical reconfiguration of EM devices has become more accessible due to the recent additive manufacturing developments and has shown potential toward expanding functionalities of conventionally geometrically static devices [33]–[35].

In this work, we perform optimization in an origami design space to achieve a desired frequency response from an origami frequency selective surface (FSS). Typical FSSs consist of a thin, flat dielectric substrate with a periodic array of conductive traces used to create pass or stop bands for electromagnetic signals in prescribed frequency ranges. The literature offers a rich variety of conductive trace and packing designs [36]. Several of those design variations were considered in our previous studies and were combined with the Miura-ori fold pattern to create foldable frequency tuning FSSs [27]. In this study, we chose rectangular strips (dipoles), as they constitute some of the simplest FSS designs, and the study can focus on the effect of incorporating folding into the FSS design.

To demonstrate the variety of EM responses in our chosen design space we have included example fold pattern unit cells and their simulated transmission responses in Fig. 1. The
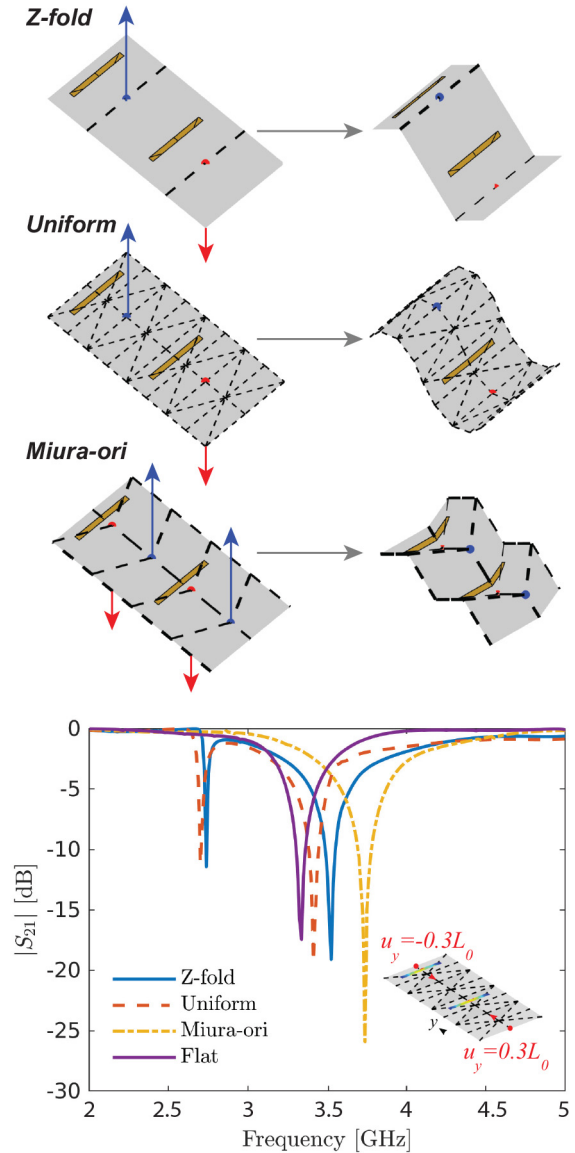
FIGURE 1. Tuning EM Performance with Origami Folding. Three representative origami fold patterns: Z-fold, uniform (wave), and Miura-ori. The fold patterns and out-of-plane forces (referred to as α and β design variables) on the left result in the folded structures on the right. Corresponding $|S_{21}|$ transmission curves and an image of the surface currents on the dipoles in the flat state are below.

frequency response of the dipole-based FSS at a flat state has a minimum transmission coefficient $|S_{21}|$ at $f_0 = 3.34$ GHz at which incoming signals are blocked due to the dipoles experiencing a current flow. The three folding examples – Z-fold, uniform (wave), and Miura-ori – are all defined by the stiffness of 33 folds (modulated in this manuscript through design variable α) and 7 out-of-plane perturbation forces along the center fold line (modulated in this manuscript through design variable β). As the substrate folds, the conductive dipole traces conformally move with the surface. The folding motion and change in distance between neighboring dipole elements results in a frequency shift due to mutual coupling and capacitive loading. The transmission
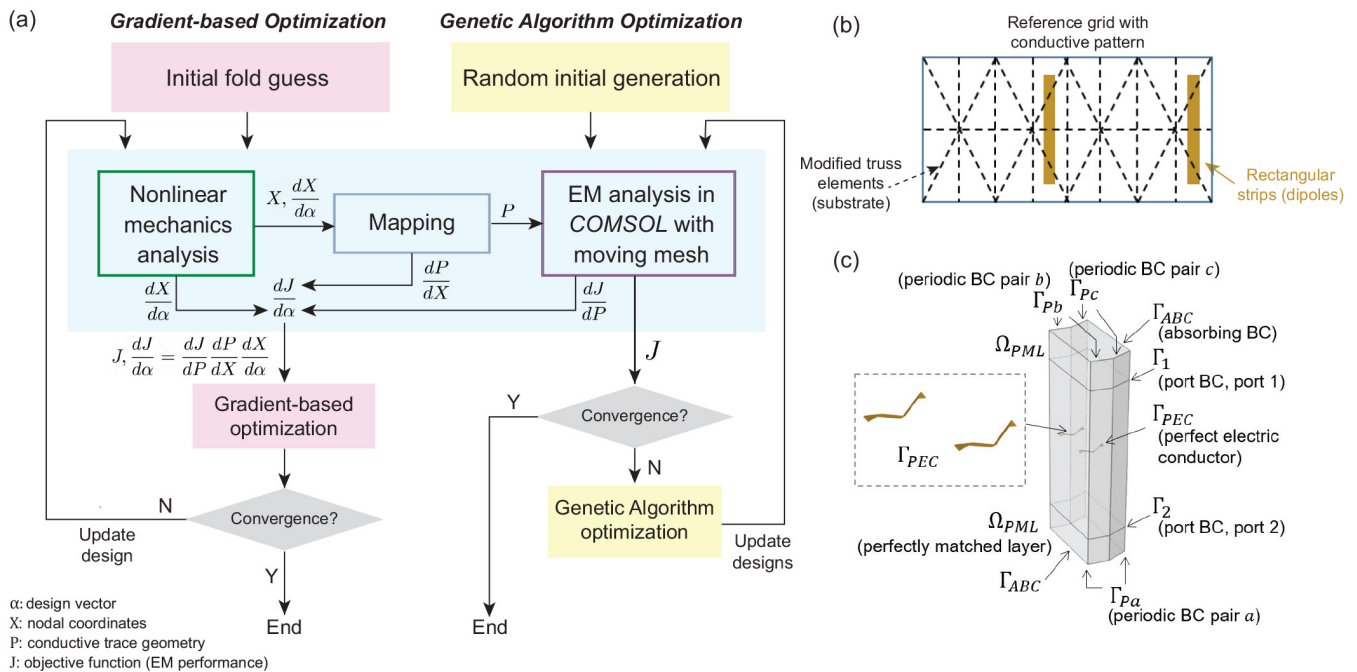
FIGURE 2. Coupling Mechanics and EM for Origami FSS Design. (a) Flowchart of the design optimization process for both gradient-based and genetic algorithm methods. (b) Fold pattern unit cell with conductive traces. (c) *COMSOL RF Module* simulation setup with Floquet boundary conditions and example folded conductive traces.

response of the three folded states can be seen compared to one another and the flat state. This comparison shows how minor changes in the physical form of the unit cell can result in significant impact on the EM performance. This parameterized form provides a convenient model for the concurrent optimization of mechanics and electromagnetics.

Two topology optimization methods are introduced in this study to find an origami crease pattern achieving a specified upward or downward frequency tuning of an FSS through folding. This work optimizes the local stiffness of the substrate bearing printed RF devices (dipoles) to enable fold-driven EM functionality, as summarized in Fig. 2. The mechanics of a foldable sheet is modeled as a network of truss elements with distributed torsion springs across adjacent facets, as illustrated in Fig. 2 (b) and demonstrated in Fig. 1 examples. A segment with a soft torsion spring indicates a fold line; one with a hard torsion spring indicates a facet. A distribution of soft and hard torsion springs constitutes a crease pattern topology. The folded configuration is found by carrying out a nonlinear simulation of a patterned sheet, loaded by input forces. The nonlinear mechanics formulation used here was developed by Gillman *et al.*, and is described in detail in [37]. This formulation based on the geometric nodal positions is advantageous for implementing position-based constraints, such as periodic boundary conditions (BCs) for simulating tessellations as shown in Fig. 2(c).

Electrically conductive patterns are selected and positioned on the unit cell of the foldable sheet to create an RF device. Dipoles are utilized in this study to help build intuition for the design space, but the design methodology

is compatible with arbitrary shapes. *COMSOL RF Module* is used to carry out the numerical evaluation of each origami design for its electromagnetic performance through full-wave solutions to Maxwell's equations in the frequency domain. *COMSOL* is a commercial finite element analysis (FEA) package and is chosen based on its flexible implementation to handle complex geometries and sensitivity analysis availability. More computationally efficient reduced order models, such as equivalent circuits [38], [39], would be ideal for quick evaluations of a large number of design options or analytically identifying the optimal design. However, reduced order models can artificially limit the design space, especially in a situation when the spatial tuning mechanisms are not well understood, and would also limit the conductive element geometries to regular shapes. Other numerical EM solution methods that can handle inhomogeneous media or complex geometries, such as the finite difference time domain methods and the method of moments, are viable alternatives to FEA and their use for topology optimization of RF devices is often seen in literature [40]–[43].

The rest of this article discusses implementing the proposed design method for origami FSSs using two optimization techniques – gradient-based and genetic algorithms. These two techniques both use the mechanics and EM analysis to explore the parameterized design space and optimize the mechanical form to achieve a desired EM-based objective. This is posed as a design method study through multiple case studies. Lastly, we highlight the complexity of EM origami by visualizing "performance islands" in the design space where the local optima tend to occur. The proposed methods, and qualitative characterization of the EM origami design landscape, are

applicable for RF devices other than FSSs and can also be adapted and expanded to include additional multiphysics applications.

II. ANALYSIS METHOD

The performance evaluation of each foldable FSS design consists of two parts: 1) mechanics analysis of the substrate to study the folding behavior; and 2) electromagnetic analysis of the folded FSS. The computational domain, element types and relevant material properties for each analysis are different, but the two analysis are coupled through the shared substrate geometry. While the substrate provides the supporting structure for the device and is important in the mechanics analysis, its thickness t is assumed to be very thin relative to the EM wavelength of interest ($t < \lambda/100$) and is omitted from the EM model to reduce the computational burden while sacrificing some accuracy on capturing the impact of the substrate. The readers are referred to [26] for a computational comparison of an FSS with and without a substrate.

A. NONLINEAR MECHANICS ANALYSIS

A nonlinear mechanics analysis based on truss elements with torsional stiffness is used to analyze the origami tessellations. This model was first introduced by Schenk and Guest [44] and has been extended to handle large geometric nonlinearity in recent works [37], [45]. The model is adopted here for its efficient mechanics analysis of foldable structures and is composed of a network of truss elements with torsional springs across all folds. The truss-based model, its nonlinear implementation and the general BC treatment are described briefly for completeness.

TRUSS-BASED ORIGAMI MODEL

The total energy, Π, of each element within a networked truss structure is described as the difference between the internal energy U and the external energy P_{ex}:

$$\Pi = U - P_{ex} = l_0 \int_0^1 \left(\frac{1}{2}EA\epsilon^2 + \frac{1}{2}Gh(\phi - \phi_0)^2\right)d\zeta - P_{ex} \tag{1}$$

where the first term in the integral is the energy contribution from the axial strain ϵ; the second term comes from the fold energy stored in the torsional spring with torsional spring constant G (per unit length). The Young's modulus, cross sectional area and the rest length of the truss element are denoted by E, A and l_0, respectively. The position vectors X_1, X_2 are used to calculate the strain as $\epsilon = (|X_1 - X_2| - l_0)/l_0$. The fold angle displacement $\phi(X_1, X_2, X_3, X_4) - \phi_0$ is defined through geometric relations of the two adjacent triangular facets as illustrated in Fig. 3. A penalty function, $h = C(\phi/\pi)^B + 1$, is used to scale the energy contribution of the fold to introduce an energy barrier near closure to avoid self-contact of adjacent facets across the fold. A constant scalar C and an even integer B are introduced to adjust the
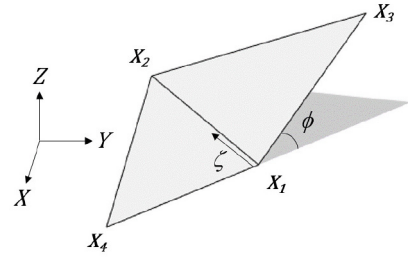
FIGURE 3. Each fold line is defined by five truss members. The coordinates of the four nodes X_1, X_2, X_3, X_4 are used to calculate the fold angle ϕ.

relative magnitude of the fold energy and the sharpness of the energy barrier, respectively. The integration is performed over the length of the element, whose coordinates can be converted into a natural coordinate $\zeta \in [0, 1]$. The external energy P_{ex} is defined as

$$P_{ex} = F_1^T \cdot u_1 + F_2^T \cdot u_2 \tag{2}$$

where $u_i = X_i - X_i^0$ and $F_i = [F_{Xi}, F_{Yi}, F_{Zi}]^T$ are the displacement vector and the external force components at node i.

The principle of minimum potential energy is used to determine the equilibrium state of the origami structure. The resulting nonlinear system of equations

$$R_i = \frac{\partial \Pi}{\partial X_i} = 0$$
$$= l_0 \int_0^1 \left(\frac{1}{2}EA\frac{\partial}{\partial X_i}\epsilon^2\right.$$
$$\left. + \frac{1}{2}G\frac{\partial}{\partial X_i}\left(h(\phi - \phi_0)^2\right)\right)d\zeta - F_i \tag{3}$$

is linearized as

$$R_i \approx R_i^0 + \nabla R_i^0 \Delta X = 0 \tag{4}$$

and solved iteratively using a Newton-Raphson (NR) scheme. The tangent term ∇R_i is obtained as

$$\nabla_l R_i = R_{i,l}$$
$$= l_0 \int_0^1 \left(\frac{1}{2}EA\frac{\partial^2}{\partial X_i X_l}\epsilon^2\right.$$
$$\left. + \frac{1}{2}G\frac{\partial^2}{\partial X_i X_l}\left(h(\phi - \phi_0)^2\right)\right)d\zeta \tag{5}$$

The readers are referred to [37] for details of the formulation, the implementation of the solution scheme, and the Lagrange multiplier approach for enforcement of the periodic BCs.

B. ELECTROMAGNETIC ANALYSIS

To evaluate the EM performance of a folded FSS in *COMSOL* using the time-harmonic electric field formulation, the vector Helmholtz equation:

$$\nabla \times \left(\frac{1}{\mu_r}\nabla \times \vec{E}\right) - k_0^2 \epsilon_r \vec{E} = 0 \tag{6}$$

is solved to find the electric field distribution $\vec{E}$ within a computational domain that contains the FSS. Vacuum is assumed

for the medium occupying the computational domain, so the relative permittivity ϵ_r and permeability μ_r are set to unity. The vacuum wavenumber $k_0 = 2\pi f/c_0$, is dependent on the frequency of interest f, and c_0 is the speed of light in vacuum. The EM properties of the conductive dipole prints are modeled by assigning perfect electric conductor (PEC) boundary conditions on the corresponding surfaces. This assumes the use of a good conductor such as copper or silver with a negligible resistive loss in the RF range. The coordinates of the folded substrate vertices, expressed as X in Fig. 4, are used to find the deformed dipole surfaces that follow the substrate deformation using a mapping function $\boldsymbol{p} = \boldsymbol{p}(X)$. Details of the mapping function are described in the next section. The model makes use of the periodicity of the FSS design to reduce the computational burden by using Bloch-Floquet periodic BCs:

$$\vec{E}(X + L) = e^{-j\boldsymbol{k}\cdot\boldsymbol{L}}\vec{E}(X) \tag{7}$$

on the side boundary pairs Γ_{Pa}, Γ_{Pb}, Γ_{Pc} in Fig. 2(c). Here X is the position vector, $\boldsymbol{L}$ denotes a tiling vector of the periodic cell, and $\boldsymbol{k}$ refers to the wave vector, whose magnitude is the vacuum wavenumber k_0 and is oriented in the wave propagation direction. Port boundary conditions are used to excite the domain with a wave propagating downward, in the negative z-direction, with the electric field aligned along the x-direction, which reduces the Bloch-Floquet periodic BCs to a simpler form:

$$\vec{E}(X + L) = \vec{E}(X) \tag{8}$$

without the phase factor $e^{-j\boldsymbol{k}\cdot\boldsymbol{L}}$. The computational domain is truncated using absorbing boundary conditions (ABCs) at the top and bottom surfaces Γ_{ABC}, as indicated in Fig. 2(c). Perfectly matched layers (PMLs) are used to suppress artificial reflections at the port boundaries. The readers are referred to [46], [47] for the finite element formulation of these BCs and the PMLs, and detailed discussions are omitted here for brevity, except to note that these are formulated to truncate the computational domain while reducing artificial reflections from the boundaries.

The electric field distribution is used to compute the quantities useful for evaluating the FSS's performance: transmission and reflection coefficients, S_{21} and S_{11}, respectively, as

$$S_{21} = \frac{\int_{\Gamma_2} \vec{E} \cdot \vec{E}^* d\Gamma}{\int_{\Gamma_1} \vec{E}_{in} \cdot \vec{E}_{in}^* d\Gamma}, \quad S_{11} = \frac{\int_{\Gamma_1} \left(\vec{E} - \vec{E}_{in}\right) \cdot \vec{E}^* d\Gamma}{\int_{\Gamma_1} \vec{E}_{in} \cdot \vec{E}_{in}^* d\Gamma} \tag{9}$$

where $\vec{E}_{in}$ refers to the input electric field, and $\vec{E}$ is the computed electric field while $\vec{E}^*$ is its complex conjugate. The performance of a stop band FSS may be illustrated by plotting the magnitude of the transmission coefficient $|S_{21}|$ over a range of frequencies. The operating frequency of this device is found as a range in which $|S_{21}|$ is below -10dB. The logarithmic scale (dB) is used to display $|S_{21}|$ with the
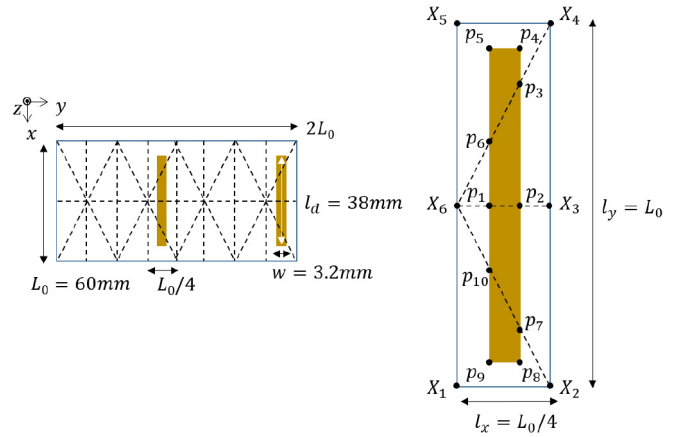

FIGURE 4. Mapping between an origami substrate with fold lines and dipoles is defined using the coordinates of truss end nodes X and dipole markers p.

following conversion.

$$|S_{21}|_{dB} = 10\log|S_{21}|. \tag{10}$$

C. MAPPING FUNCTION

Figure 4 illustrates the mapping function $\boldsymbol{p}(X)$ that describes the surface geometry of dipoles (colored rectangular strips) of width w and length l_d following a folded substrate configuration X defined by the coordinates of the vertices. In Fig. 4, dotted lines indicate segments across which torsional springs are inserted. The coordinates of ten points $\boldsymbol{p}_1^e, \ldots, \boldsymbol{p}_{10}^e$ are computed using six vertices of triangular facets, $X_1^e, \ldots, X_6^e$ for each dipole e.

$$\boldsymbol{p}_1 = X_6 + \frac{1}{2}(l_x - w)\hat{\boldsymbol{i}}_1$$

$$\boldsymbol{p}_2 = \boldsymbol{p}_1 + w\hat{\boldsymbol{i}}_1$$

$$\boldsymbol{p}_3 = X_6 + (l_1 + l_3)\hat{\boldsymbol{j}}_1$$

$$\boldsymbol{p}_4 = \boldsymbol{p}_3 - \left[\frac{1}{2}l_d - (l_1 + l_3)sin\theta\right]\hat{\boldsymbol{j}}_2$$

$$\boldsymbol{p}_5 = \boldsymbol{p}_6 - \left[\frac{1}{2}l_d - \frac{1}{4}l_y\left(1 - \frac{w}{l_x}\right)\right]\hat{\boldsymbol{j}}_2$$

$$\boldsymbol{p}_6 = X_6 + l_1\hat{\boldsymbol{j}}_1$$

$$\boldsymbol{p}_7 = X_6 + (l_1 + l_3)\hat{\boldsymbol{j}}_3$$

$$\boldsymbol{p}_8 = \boldsymbol{p}_7 - \left[\frac{1}{2} - (l_1 + l_3)sin\theta\right]\hat{\boldsymbol{j}}_4$$

$$\boldsymbol{p}_9 = X_1 + \frac{1}{2}(l_x - w)\hat{\boldsymbol{i}}_4 + \frac{1}{2}(l_x - l_d)\hat{\boldsymbol{j}}_4$$

$$\boldsymbol{p}_{10} = X_6 + l_1\hat{\boldsymbol{j}}_3 \tag{11}$$

where $\hat{\boldsymbol{i}}$ and $\hat{\boldsymbol{j}}$ are unit vectors defined to specify local coordinates on the four triangular facets:

$$\hat{\boldsymbol{i}}_1 = \frac{(X_3 - X_6)}{\|X_3 - X_6\|}, \quad \hat{\boldsymbol{j}}_1 = \frac{(X_4 - X_6)}{\|X_4 - X_6\|}$$

$$\hat{\boldsymbol{i}}_2 = \frac{(X_4 - X_5)}{\|X_4 - X_5\|}, \quad \hat{\boldsymbol{j}}_2 = \frac{(X_6 - X_5)}{\|X_6 - X_5\|}$$

$$\hat{\boldsymbol{j}}_3 = \frac{(X_2 - X_6)}{\|X_2 - X_6\|}$$

$$\hat{\boldsymbol{i}}_4 = \frac{(\boldsymbol{X}_2 - \boldsymbol{X}_1)}{\|\boldsymbol{X}_2 - \boldsymbol{X}_1\|}, \quad \hat{\boldsymbol{j}}_4 = \frac{(\boldsymbol{X}_6 - \boldsymbol{X}_1)}{\|\boldsymbol{X}_6 - \boldsymbol{X}_1\|} \tag{12}$$

and

$$l_x = \frac{1}{4}L_0, \quad l_y = L_0, \quad l_1 = \frac{l_x - w}{2\cos\theta}, \quad l_3 = \frac{w}{\cos\theta},$$
$$\theta = \arctan\left(\frac{l_y/2}{l_x}\right) \tag{13}$$

Note that this mapping function is valid only for a model that does not involve facet stretching, and a more general mapping would be required for stretchable devices. In this work, structural properties of the substrate are set such that facet stretching is negligible.

III. DESIGN OPTIMIZATION

The goal of the design optimization problem is to find an origami-foldable FSS design that shifts the target filter frequency when folded. This is achieved by optimizing the fold stiffness and input loading distributions over a prescribed reference origami crease pattern, such that the transmission coefficient at a target frequency is minimized. While the design is ultimately evaluated based on the EM performance, the design description relies on the fold stiffness distribution and the loading condition, which are structural properties. In order to use a gradient-based optimization algorithm, sensitivity analysis of both EM and structural responses are carried out, and the chain rule is used to relate the EM performance sensitivity to the structural design parameters. The method of moving asymptotes (MMA), a gradient-based optimization algorithm developed by Svanberg [48], and a genetic algorithm are both explored as methods to find optimal solutions.

A. OBJECTIVE FUNCTION

The design goal is to tune the operating frequency of a band-stop FSS through folding. Again, this is done by minimizing the transmission coefficient at the target frequency. In comparison to more sophisticated objective choices used to control the system behavior over a range of frequencies (e.g., an objective based on the frequency response of a dynamical system represented using Padé approximants in [49]), the chosen objective J can be evaluated at a relatively low computational cost, as seen in [50], [51].

$$J = \left|S_{21}\left(f^*\right)\right|^2. \tag{14}$$

B. DESIGN VARIABLES

Similar to our previous works in origami-based mechanism design problems [52], [53], an origami design is described first by defining a reference crease pattern (as seen in Fig. 4) and assigning a variable fold stiffness G along each segment s. Here a small fold stiffness value ($G = 10^0$) corresponds to a foldable segment, while a large value ($G = 10^4$) refers to a rigid facet. An interpolation function

$$G = 10^{\bar{\alpha}_1 + \alpha_s(\bar{\alpha}_2 - \bar{\alpha}_1)} \tag{15}$$

is used to describe the variable fold stiffness G with $\bar{\alpha}_1 = 0$, $\bar{\alpha}_2 = 4$, controlled by a continuous design variable $\alpha_s \in [0, 1]$. While a continuous design variable ensures differentiability of the fold stiffness, a discrete solution is desired in practice. This improves the ability to interpret the tuning mechanisms of the predicted design and the simplicity of fabrication. A constraint on the number of soft folds, combined with the interpolation scheme in Eq. (15), biases convergence towards a binary solution. This is similar to a technique employed in structural topology optimization, where the solid isotropic material with penalization (SIMP) scheme is combined with a volume constraint to achieve clearly defined optimal topologies [54].

The origami folding is actuated through an in-plane loading applied at the outer edges of the initially flat sheet. In order to initiate folding off-flat, an additional loading in the z-direction at select nodes is applied. The selection of these out-of-plane loading conditions must be done in combination with fold stiffness distributions. A design variable $\beta_j \in [-1, 1]$ is assigned to each node j, and the out-of-plane loading condition at node j is expressed as

$$F_z^j = F_0\beta_j^P \tag{16}$$

where F_z^j refers to the z-component of the loading vector at node j, F_0 is a scaling factor, and P denotes a penalty factor. To allow for a combination of upward and downward loads, design variable β_j can take a negative or positive value, and an odd integer is chosen for the penalty factor P.

C. CONSTRAINTS

A constraint on the total number of soft folds relative to the total number of potentially foldable segments N_f:

$$g_1 = v_a \leq \sum_{s=1}^{N_f} \alpha_s/N_f \tag{17}$$

facilitates convergence of the fold stiffness distribution towards binary. This is similar to a volume constraint in a typical structural topology optimization using SIMP [54]; ensuring the number of stiff segments are larger than a fraction v_a of the total number of segments is equivalent to restricting the fraction of the soft, foldable segments to be less than a set value. This value is adjusted to control the complexity of the origami design, where a large value refers to fewer fold lines.

A constraint on the mean of squares of out-of-plane loads:

$$g_2 = \sum_{j=1}^{N_n} \beta_j^2/N_n \leq v_b^2 \tag{18}$$

is used to attain a solution with a small number of active out-of-plane loading points, using a similar strategy used for fold stiffness. Here N_n denotes the number of nodes in the structure.

D. OPTIMIZATION PROBLEM STATEMENT

The optimization problem is formally stated as follows.

$$\text{Find } \alpha_1, \alpha_2, \ldots, \alpha_{N_f}, \beta_1, \beta_2, \ldots, \beta_{Nn} \quad \text{that}$$

$$\text{Minimizes } J = \left| S_{21}(f^*) \right|^2$$

$$\text{Subject to } g_1 = v_a - \sum_{s=1}^{N_f} \alpha_s / N_f \leq 0$$

$$g_2 = \sum_{j=1}^{N_n} \beta_j^2 / N_n - v_b^2 \leq 0$$

$$0 \leq \alpha_s \leq 1, \quad s = 1, \ldots, N_f$$

$$-1 \leq \beta_j \leq 1, \quad j = 1, \ldots, N_n$$

$$R_i(X) = 0 \tag{19}$$

where $R_i(X) = 0$ refers to the governing equation of the system as described in Eq. (3), whose solution depends on the design. The objective function J is defined using the transmission coefficient S_{21} defined in Eq. (9), evaluated at the target operating frequency f^*.

E. GRADIENT-BASED OPTIMIZATION - SENSITIVITY ANALYSIS

The gradients of the objective function J with respect to the fold stiffness distribution α_s and out-of-plane loading β_j are computed using sensitivities from both nonlinear mechanics and EM analysis as

$$\frac{dJ}{d\alpha_s} = \frac{dJ}{d\tilde{p}} \frac{d\tilde{p}}{dp} \frac{dp}{dX} \frac{dX}{d\alpha_s} \tag{20}$$

and

$$\frac{dJ}{d\beta_j} = \frac{dJ}{d\tilde{p}} \frac{d\tilde{p}}{dp} \frac{dp}{dX} \frac{dX}{d\beta_j}. \tag{21}$$

The first gradients $\frac{dJ}{d\tilde{p}}$ are extracted using the moving mesh and sensitivity analysis mode in the *COMSOL Optimization Module* during the EM analysis. By setting the EM computational domain as the "free deformation" domain, the sensitivity of the objective function J with respect to the mesh motion becomes available to be evaluated at desired locations. The gradients $\frac{dJ}{d\tilde{p}}$ are computed at mesh points on dipole surfaces, $\tilde{p}$.

The second gradients $\frac{d\tilde{p}}{dp}$ are defined to map the extracted sensitivity computed at nodes $\tilde{p}$ created during meshing for the EM analysis in *COMSOL* onto dipole mapping nodes p, as defined in Fig. 4. While points $\tilde{p}$ and p should coincide in theory, their locations deviate slightly due to machine errors in meshing. A gradient mapping function

$$\frac{d\tilde{p}}{dp} = e^{-a\|\tilde{p}-p\|} \tag{22}$$

is used to smoothly account for any deviations between $\tilde{p}$ and p locations. Perfectly coincident $\tilde{p}$ and p result in $\frac{d\tilde{p}}{dp} = 1$, and a slight deviation leads to a reduced value, whereas a large deviation produces a value close to zero, diminishing the sensitivity contribution of a point $\tilde{p}$ far away from the

reference dipole mapping point p. Constant a is set to adjust the sharpness of the gradient mapping. Throughout this work, $a = 100/l_d$ is used, so that a point $\tilde{p}$ away from p by a significant fraction (greater than 1%) of the dipole length l_d has a negligible sensitivity contribution.

The third gradients are used to map the gradients at dipole nodes onto the triangular origami facet nodes X. These gradients can be obtained by calculating derivatives of the dipole mapping expressions in Eq. (11) with respect to X. Finally, gradients $\frac{dX}{d\alpha_s}$, $\frac{dX}{d\beta_j}$ are computed during the mechanics analysis and used here to relate the objective function based on the transmission coefficient to structural properties described through α_s and β_j.

Following the sensitivity analysis used for mechanism design problems in [53], the last gradients $dX/d\alpha_s$ are determined using the direct method in solving the following system of equations

$$R_{i,l} \frac{dX_l}{d\alpha_s} = -\frac{\partial R_i}{\partial \alpha_s}, \quad i, l = 1, \ldots, N_{dof} \tag{23}$$

using the residual R_i and the tangent term $R_{i,l}$ derived in Eqs. (3) and (5), where N_{dof} is the number of degrees of freedom in the structural analysis.

F. GENETIC ALGORITHM OPTIMIZATION

A design method based on a genetic algorithm optimization approach is used to perform a comparative study for one of the example cases. For this study, the genetic algorithm was initialized with a randomized population of 100 uniform fold pattern designs. The representative genomes were 40-element vectors containing 33 values, α_s, modulating the fold line stiffness G [see Eq. (15)] and 7 values, β_j, modulating the out-of-plane perturbation load [see Eq. (16)] at nodes along the center of the pattern.

Each design is modeled and evaluated using the outlined nonlinear mechanics analysis. If a combination of α_s and β_j fails to solve a single nonlinear mechanics step, it is replaced by a flat, unfolded sheet in the population along with its performance. The resulting generation is then evaluated in *COMSOL*. In order to reduce the computational time, the 'parametric sweep' feature in COMSOL was used, which allows parallel simulations of each design during a single GA generation. The genomes of the best performers from each generation are crossed and mutated to create a subsequent generation of 100 designs. This process is repeated until the default MATLAB Global Optimization stopping criteria for GAs are met.

IV. NUMERICAL EXAMPLES

To demonstrate the utility of the introduced origami design optimization methods, two problems of finding origami patterns to tune the operating frequency of a dipole-based FSS are discussed. The FSS used in this work was designed to operate in the S-band (2-4 GHz), but the same design principles can be used for an FSS in a different operating frequency range by scaling the physical dimensions of the device. The

TABLE 1. Parameters used to perform the mechanics and electromagnetic analyses of the origami FSS.

Mechanics Parameters	A	E	B	C	$G\|_{\alpha_s=0}$	$G\|_{\alpha_s=1}$
	1.0mm^2	10^3GPa	100	10.0	1.0N	$1.0\times10^4\text{N}$
EM Parameters	l_d	w	L_0			
	38mm	3.2mm	60.0mm			

goal of the optimization problem is to find fold stiffness and force distributions that result in a low transmission level at a new target operating frequency f^*.

The periodic setup in the EM analysis requires that the underlying origami structure also satisfies periodic BCs. This is implemented in the mechanics analysis following the Lagrange multiplier approach, as described in [37]. An in-plane loading is applied inward at the center nodes of the outer edges of the periodic unit as indicated by the red arrows on the flat pattern inset in Fig. 1, with the target displacement set at $0.3L_0$, along with the out-of-plane loading controlled by design variables. The in-plane loading condition is implemented using a displacement-controlled scheme with 100 linear loading steps. While the target displacement value influences the FSS performance significantly, a fixed value is selected based on our prior studies and used here, to focus the design process on finding an effective fold pattern.

In the examples considered here, symmetry about the horizontal center line (along the y-axis in Fig. 4) is assumed for the fold pattern, and the out-of-plane actuation is only applied at nodes along the center line. With the symmetry assumption, the number of fold lines and actuation locations are 33 and 7 respectively, resulting in a total of 40 design variables. A uniform fold stiffness distribution with upward and downward input loading at two nodes along the center line are used together as an initial guess, corresponding to fold line fraction $v_a = 0.5$ and actuator fraction $v_b = 0.3$, unless specified otherwise. Other parameters used in the examples are summarized in Table 1.

The optimization step size for the MMA gradient-based algorithm is set to 0.05 [note that all the design variable ranges are normalized, see Eq. (19)], but reduced by half if the optimization algorithm MMA returns a design update that produces a design with more than 1dB increase in $|S_{21}(f^*)|$, around particularly sensitive design regions. The GA is configured as described above (default operators and convergence criteria in MATLAB's implemented GA), and sets the objective function to the equivalent of the undeformed flat state if the design yields an incompatible one, i.e., if the nonlinear mechanical analysis fails to converge.

A. GRADIENT-BASED – UPWARD FREQUENCY TUNING

A target frequency of $f^* = 3.75$ GHz is used for the first example. The objective function $J = |S_{21}(f^*)|^2$ is evaluated at this frequency.

The iteration history of the objective function plotted in Fig. 5(a) shows a clear design improvement in the first few iterations, indicating a lower transmission coefficient at the target frequency $f^* = 3.75$ GHz. The frequency responses
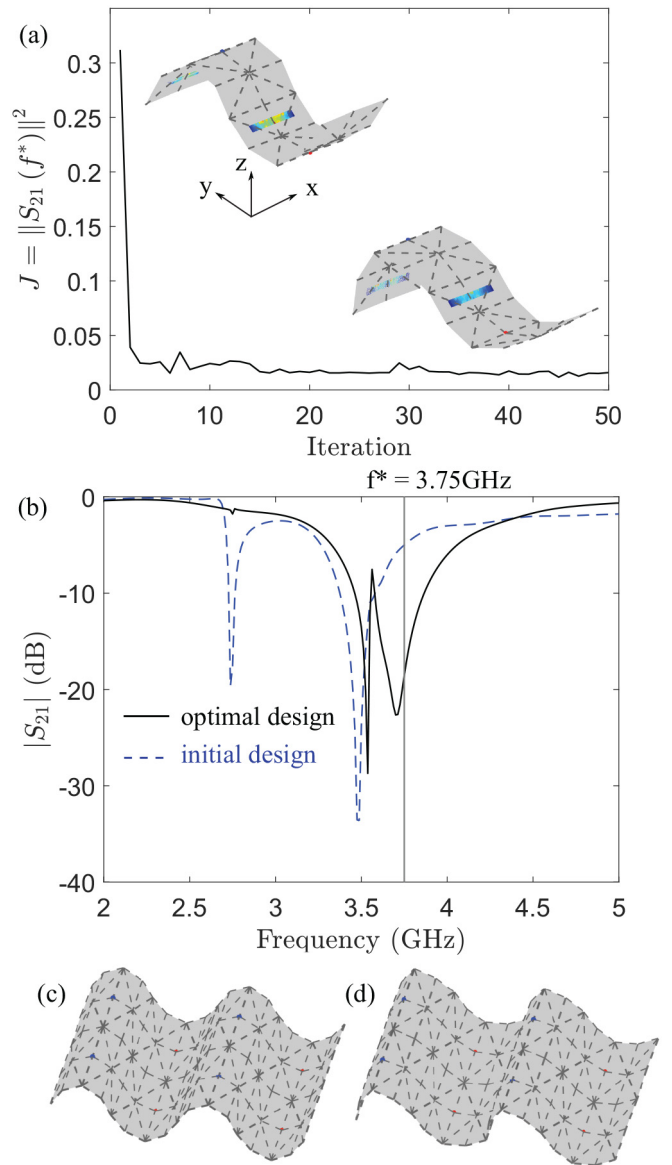
FIGURE 5. Summary of results for the MMA upward frequency tuning example. (a) Iteration history with initial and final configurations, with color plot of E-field surface currents overlaid; (b) frequency responses of the FSS with initial and optimal configurations; (c) tessellation of initial design; (d) tessellation of optimal design.

of the initial (dotted line) and optimal design (solid line) are shown in Fig. 5(b), where a resonance shift closer to the target frequency $f^* = 3.75$ GHz is observed. The initial and optimal configurations with the surface current distributions on the dipoles are shown as insets in Fig. 5(a). Both constraints are satisfied throughout the optimization process.

The side views of the initial and optimal configurations are shown in Fig. 6, where the shortened in-plane dipole distance in the optimal configuration is observed. The frequency tuning obtained in this example can be explained using our observations in [28], where an upward shift in resonance is seen when a corrugated FSS is folded to shorten the distance between the dipole pair [see Fig. 7(a), red circles for a frequency trend and (b) for a sketch of the dipole separation
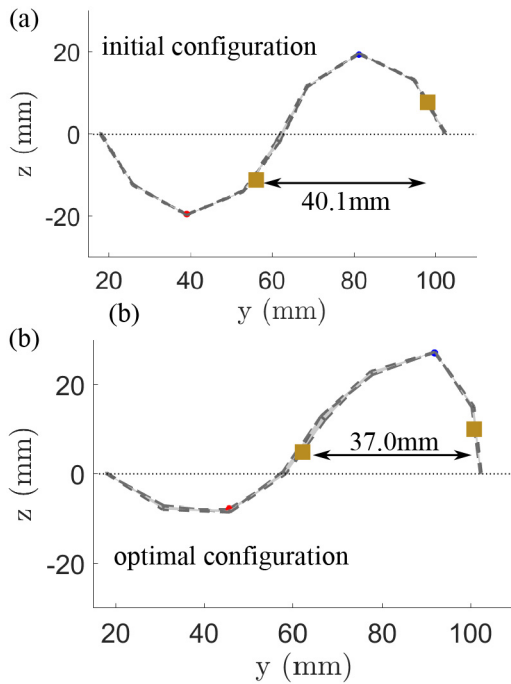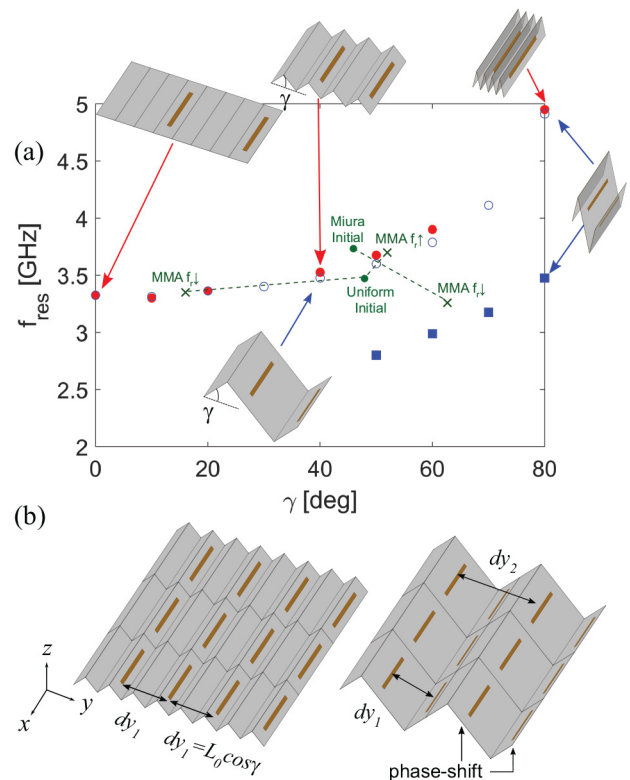
FIGURE 6. Side view of the (a) initial and (b) optimal configurations for the first example with the dipole locations (indicated as squares).


FIGURE 7. Resonant frequency tuning trend. (a) Resonant frequency vs. dipole separation distance for simple corrugations and frequency tuning during the optimization process (green dots: resonance at initial Uniform and Miura designs; crosses: resonance at optimal MMA designs for Uniform Downward ($f_r \downarrow$), Uniform Upward ($f_r \uparrow$), and Miura Downward frequency tuning case studies); (b) sketches of corrugated and Z-shaped tessellations.

distance dy_1]. This trend is attributed to a smaller Floquet periodicity in the *y*-direction. Although the qualitative nature of the folding pattern did not change between the initial and optimal configurations, the optimization process took advantage of this mechanism and re-arranged the folds to adjust the relative dipole locations to shift the resonance close to the target frequency. The green cross marked "MMA Uniform Upward" in Fig. 7 (a) shows the resonant frequency of the optimal configuration, plotted at the equivalent γ value based on the in-plane dipole distance $dy = L_0 cos\gamma$; the other end of the dotted line shows the data for the initial configuration. The frequency shift achieved through optimization generally follows the frequency trend of the corrugated fold pattern but at a higher rate of change.

Another interesting behavior seen in the frequency response in Fig. 5(b) is that there are two resonances in both initial and final configurations. This is attributed to the different dipole heights, producing a relative phase shift, creating different dipole pairings with corresponding periodicity lengths. The effect of an increasing dipole height difference also observed in the Z-shaped folding pattern [28], as summarized in Fig. 7. While the dominant resonance (blue circles) shifts upward through folding, another resonance (blue squares) appears when the FSS is folded beyond a certain extent ($\alpha = 40°$). The difference in the dipole heights then becomes large enough to create two distinct dipole pairing distances, dy_1 and dy_2 in Fig. 7(b), right. The frequency response of the optimal design exhibits a combination of these effects, where the main resonance is shifted upward due to a shorter in-plane distance, and the

secondary peak is almost merged to the main peak as the height difference becomes small.

B. GRADIENT-BASED – DOWNWARD FREQUENCY TUNING

A target frequency of $f^* = 3.25$ GHz is used for the second example. Based on our previous studies, there are two known principles by which a folding leads to an upward frequency shift. One due to a shorter distance between paired conducting elements, as discussed in the previous example; another caused by an apparent shortening of an element with respect to the incident field due to a fold along the element [27]. Due to these mechanisms, a means to shift the frequency downward is not immediately apparent. This example showcases the effectiveness of the design method in systematically finding an origami pattern that achieves a desired frequency tuning.
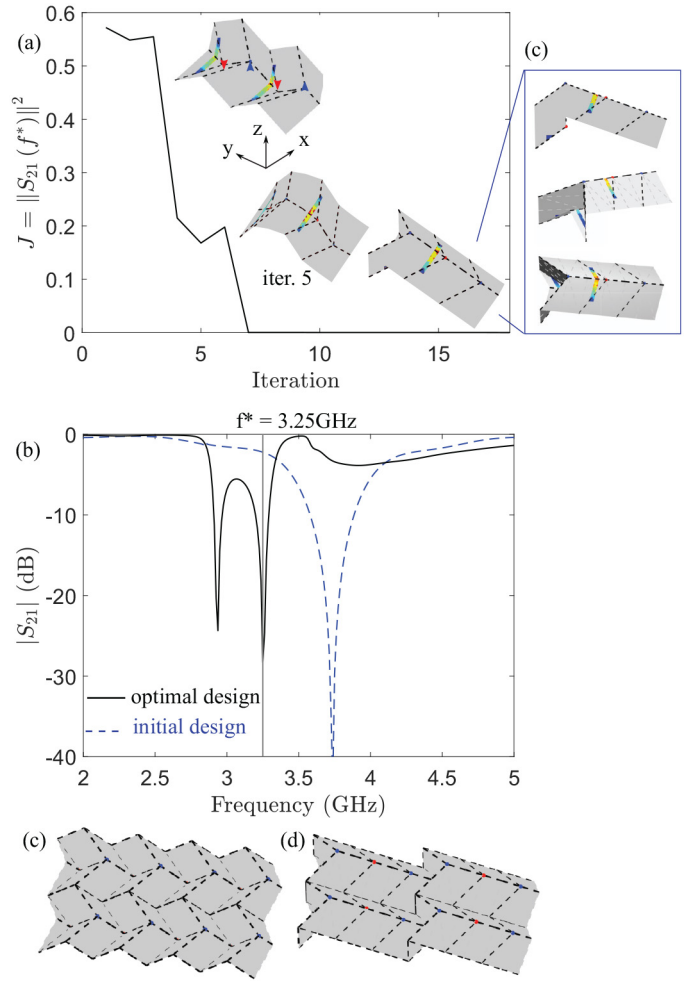
A uniform initial guess is used in the first downward shifting case study. Again, the performance improves significantly in the first few iterations, as seen in Fig. 8(a). An optimal configuration is a shallow sine-wave shape, resulting in a larger dipole distance and a slight downward resonance shift to 3.35 GHz, which is slightly above the flat-state resonant frequency of 3.34 GHz. This configuration is achieved by adjusting fold stiffness and actuation distributions such
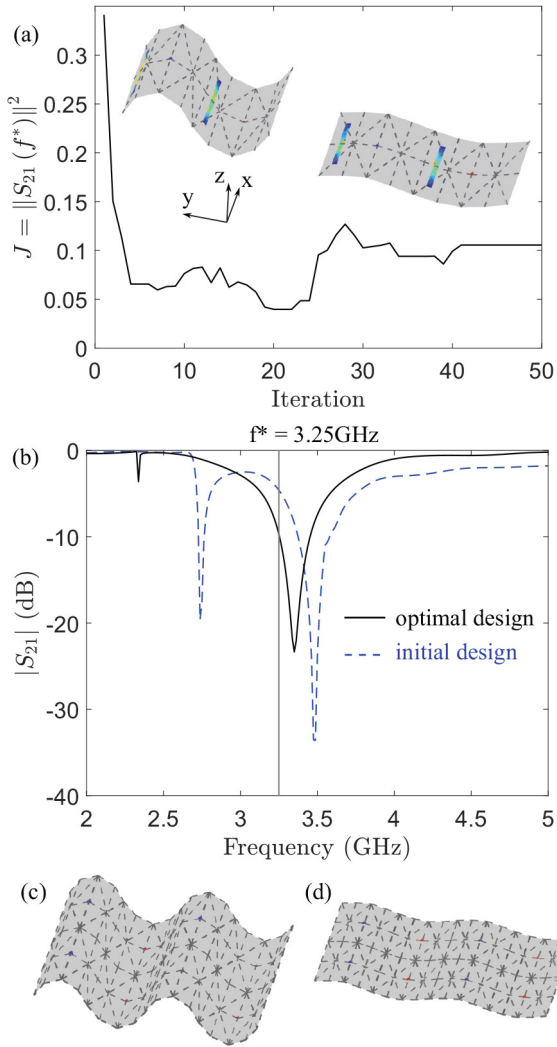
FIGURE 8. Summary of results for the MMA downward frequency tuning example with uniform initial guess. (a) Iteration history with initial and final configurations and color plot of E-field surface currents overlaid (b) frequency responses of FSSs folded following initial and optimal designs; (c) tessellation of initial design; (d) tessellation of optimal design.

FIGURE 9. Summary of results for the MMA downward frequency tuning example with Miura-ori initial guess. (a) Iteration history with initial and final configurations and color plot of E-field surface currents overlaid; (b) frequency responses of FSSs folded following initial and optimal designs; (c) optimal configuration from different view angles; (d) tessellation of initial design; (e) tessellation of optimal design.

that the structure only loads up to 9% of the target in-plane displacement, leaving a large distance between dipoles. The resonant frequencies of the initial and optimal configurations are plotted at equivalent γ values in Fig. 7(a) and marked "MMA Uniform Downward". This design uses the frequency tuning mechanism observed in the previous example in reverse, again following the general trend of the frequency tuning of the corrugated FSS, however, the extent of the resonant frequency shift using this method is limited by the substrate length.

The same problem is solved again, this time using a Miura-ori pattern as the initial guess. The limit value for the actuation constraint is increased to $v_b = 0.7$, so that the initial actuation guess with two upward and two downward forces satisfies the constraint. The initial fold stiffness, out-of-plane actuation distributions and corresponding folded configuration are seen in the left inset of the iteration history

plot in Fig. 9(a). The optimal configuration exhibits a fold pattern with one Miura-ori unit but with the rest of the sheet flattened out [see Fig. 9(c)], producing a qualitatively different configuration and a frequency response compared to the initial configuration, as shown in Fig. 9(b). The iteration history shows the design settling into a sub-optimal design for several iterations around iteration 5, but eventually changing into a different configuration with a significant improvement in the objective. The optimal configuration obtained in this case study places the two folded dipoles at different heights, with the upper dipole being unfolded at the corners and elongating the corresponding wavelength. The height difference creates a significant phase shift between the dipole pair as in the Z-shape configuration in Fig. 7 and produces two distinct resonances. The pairing of the top dipole to one in its adjacent periodic unit, equivalent to the dy_2-pairing illustrated in Fig. 7(b), is responsible for the lower resonance at $f = 2.94$ GHz. This case study demonstrates the design method's ability to identify an origami

pattern that effectively utilizes combined tuning mechanisms based on unfolding parts of a dipole and creating a phase shift, producing a tuning trend different from those observed in simple corrugations [see "MMA Miura Downward" in Fig. 7(a)]. It is also notable that one of the resonances produced by the optimal configuration occurs at the target frequency.

As seen in Fig. 9, changes in out-of-plane loading, adjusted through β_j, produces 3 distinct shapes and a quick convergence within 7 iterations of the MMA optimization algorithm even with limited change in fold stiffness distribution. To understand further how the perturbation forces affect the folded shape of the substrate, we consider all combinations (939 simulations) of applying up to 4 out-of-plane nodal forces (out of 7 centerline node locations) to the Miura-ori fold pattern (α_s fixed to 0 and 1 corresponding to initial guess in Fig. 9). We employ t-Distributed Stochastic Neighbor Embedding (t-SNE) [55] to reduce the high dimensional data representing the configuration and design spaces to two dimensions for visualization and interpretation. Fig. 10 shows the resulting t-SNE distributions with two algorithm inputs: dipole coordinates, $\vec{p}_n$, [Fig. 10(a)] and the vector of design variables, β_j, modulating the out-of-plane perturbation force [Fig. 10(b)]. The scatter plots are colored by the difference of the dipole configuration, $\vec{p}_n$, from the known Miura-ori configuration, defined as $||\vec{p}_{miura} - \vec{p}_n||$. The resulting configurations are clearly clustered [Fig. 10(a)], representing the various configurations that can be realized for all combinations of β_j studied here. Representative inset images show the corresponding configuration for each cluster. However, these configurations are scattered when plotted over the design space manifold, visualized in Fig. 10(b). These plots also show where the data points from the gradient-based MMA optimization, colored red, fall in relation to this parametric study. The closely clustered red dots in Fig. 10(b) reveal the local nature of the design exploration performed through gradient-based optimization and the challenge of exploring the entire design space. It is also noted here that many combinations of α_s and β_j result in incompatible design variables, i.e., the nonlinear solver fails to load the structure given poor numerical conditioning and/or incompatible forces and fold line configurations. These points are colored gray in Fig. 10(b) and omitted from Fig. 10(a).
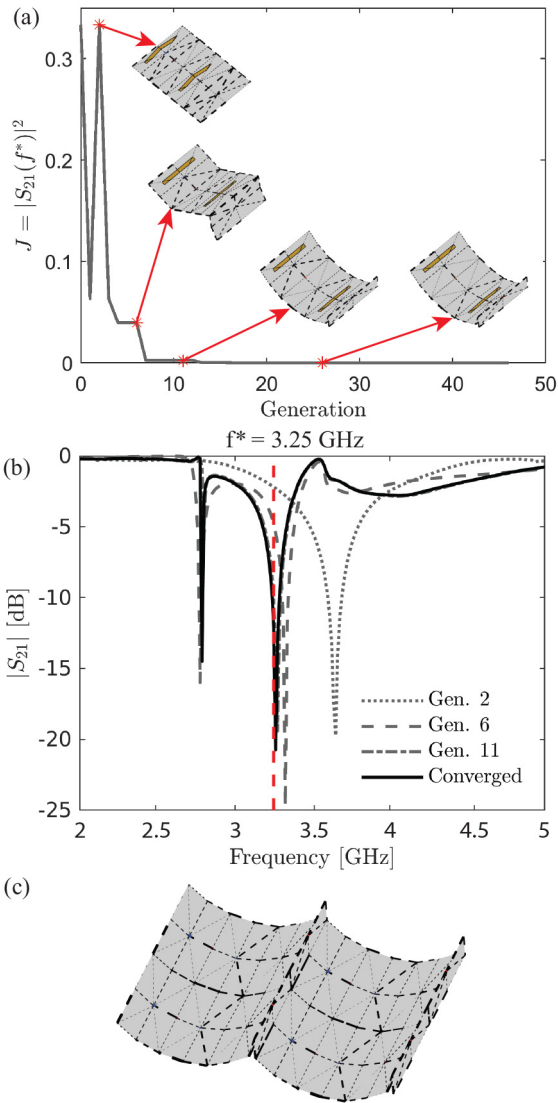
C. GENETIC ALGORITHM – DOWNWARD FREQUENCY TUNING

To expand the design space explored during the optimization process, a GA-based design method is used to solve the design problem with the downward tuning objective (as described in Section III-F). The resulting evolution of the objective function for the optimal design in each generation is presented in Fig. 11(a), and the associated frequency responses for select designs [insets from Fig. 11(a)] are presented in Fig. 11(b).
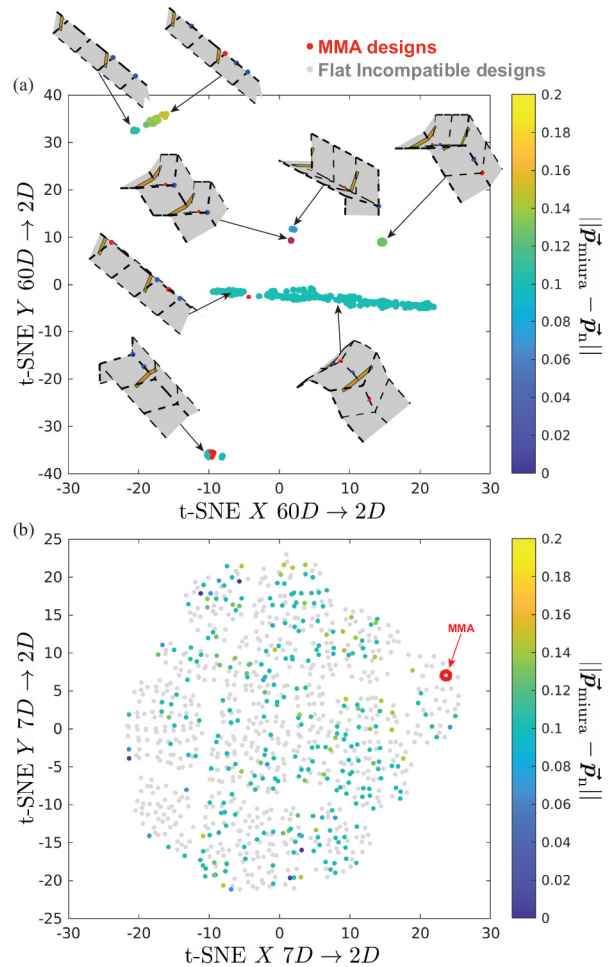
FIGURE 10. t-SNE dimensionality reductions of Miura-ori design space representation denoting the placement of the 18 MMA designs from the downward shifting Miura-ori case study. Color overlays represent the difference of the design dipole coordinate vector, $\vec{p}_n$ from the initial Miura-ori dipole coordinate vector $\vec{p}_{miura}$. t-SNE input vectors include: (a) 60-element dipole coordinate vector $\vec{p}$, (b) 7-element out-of-plane loading distribution vector β.

From the insets in Fig. 11, one can observe that while all creases are at varying levels of stiffness, only certain creases are folded significantly. The iteration history shows a similar speed of convergence to the MMA (< 10 iterations/generations). Additionally, three unique configurations appear as the best performers as the algorithm converges, with minor improvements to the configurations and objective function with later generations. While it is customary to employ discrete design variables in a GA, all 40 design variables are treated as continuous variables as in the gradient-based scheme. To further expand the design space, a symmetric design is not enforced in the GA scheme and therefore not likely to be encountered, given the random nature of the initial design variable distributions. Thus, it is not surprising that the Miura-ori designs seen in the gradient-based downward tuning example were not encountered in the GA populations. Nevertheless, the GA-based approach finds fold and actuation combinations that achieve

FIGURE 11. Summary of results for the genetic algorithm downward frequency tuning example with uniform fold initialization. (a) Iteration history of best performing designs with four design examples including the final converged design. Note 100 EM simulations per GA generation; (b) frequency responses of FSSs folded corresponding to the designs selected from the iteration history plot; (c) Tessellation of the top performer of the last generation.

desired performances without supplying a reasonable initial guess.

D. INTERPLAY OF FOLD TOPOLOGY AND FOLD PATH

The strong influence of the initial conditions is a consequence of a non-convex nature of the design optimization problem investigated in this work. While a gradient-based MMA method generally leads to an efficient design update and a faster convergence to a local optimum, experiences in our research effort indicate that the GA is capable of interrogating a wider area of the design space in finding an optimal solution, though at a much higher computational cost.

The evolution of the design variable change from the initial design plotted in Fig. 12 also shows that the design
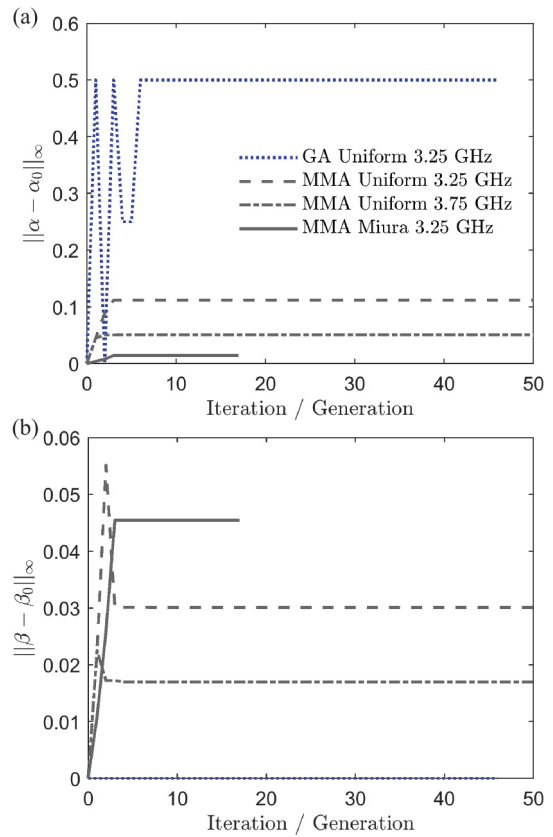
FIGURE 12. Evolution of the changes in the design variables for the (a) fold stiffness α and (b) out-of-plane actuation β, compared to the initial design.

converges to a solution within the neighborhood of the initial guess for all MMA case studies. This highlights the sensitivity of some parts of the design space with respect to the FSS performance, given the dramatically different FSS performance achieved in the optimal design of the MMA Miura-ori case study. It is worth noting that the MMA Miura-ori initialization case study seems to focus on adjusting the actuation to perturb the structure into a different shape available within the Miura-ori fold pattern; the MMA uniform initialization case studies focus more on adjusting the fold stiffnesses to obtain the desired variations of the sine-wave shape. While viewing the change in α and β values for the GA case we see a similar trend when comparing the top performer of the initial generation to all subsequent generations. In this GA case, we see that perturbation values do not change between top performers from generation to generation. However, we do see significant change in fold stiffness values. This finding shows that both MMA and GA optimizers used similar mechanisms to find an optimal solution for the downward shifting uniform initialization case. A notable difference between the two is the magnitude of that change in fold stiffness, the comparison between these two curves in Fig. 12(a) shows that the GA is better suited to find diverse solutions in the design space.

V. CONCLUSION

An origami crease topology optimization method for electromagnetic applications was introduced. The formulation used a modified-truss model to carry out the nonlinear mechanics analysis to simulate the folding of a substrate and *COMSOL RF Module* to analyze the electromagnetic performance. A geometry mapping was used to relate the structurally-relevant origami substrate geometry to the electromagnetically-relevant conductive print orientations. A gradient-based method was developed and used to optimize the fold stiffness and out-of-plane loading distributions on a substrate to tune the operating frequency of an FSS to a desired location by minimizing the transmission coefficient at the target frequency. To contrast the performance, we also considered a GA-based approach.

Numerical examples demonstrated the use of the proposed methods to achieve upward and downward frequency tuning of a dipole-based folded FSS. Upward tuning was achieved by making use of a shorter dipole coupling distance by folding a part of the substrate closer together. Downward tuning was achieved by unfolding dipole corners and adjusting the dipole height levels to create a phase shift. These examples demonstrated that the proposed method utilized the sensitivity information of the electromagnetic performance with respect to the structural properties of the origami sheet to systematically find origami designs that produced desired FSS responses. Both the gradient and GA approaches only explored small subsets of the design space given the complex relation between the fold and actuation distributions, the resulting form and the EM performance.

The proposed methods are general and may be applied to a wide variety of origami design problems, but are particularly relevant for complex problems such as electromagnetics and multiphysics problems, where intuitive origami design strategies are limited. A hybrid of a computationally efficient design procedure with an approach that can access a large design space is recommended for solving these design problems, as optimizing to functional standards such as a tailored frequency response or radiation pattern, is often a complex and non-convex problem. Based on our findings, a method capable of systematically assessing the relationship between fold patterns, actuation and their mechanical compatibility, such as the nonlinear mechanics analysis adopted in this work, is an important component of the origami design process.

REFERENCES

[1] T. Takano *et al.*, "Deployable antenna with 10-m maximum diameter for space use," *IEEE Trans. Antennas Propag.*, vol. 52, no. 1, pp. 2–11, Jan. 2004.

[2] S. A. Zirbel *et al.*, "Accommodating thickness in origami-based deployable arrays," *J. Mech. Design*, vol. 135, no. 11, 2013, Art. no. 111005.

[3] S. Jape *et al.*, "Self-foldable origami reflector antenna enabled by shape memory polymer actuation," *Smart Mater. Struct.*, vol. 29, no. 11, 2020, Art. no. 115011.

[4] F. Espinal *et al.*, "Circularly-polarised origami-inspired folding patch antenna sub-array," *IET Microw. Antennas Propag.*, vol. 14, no. 11, p. 10, 2020.

[5] D. Rus and M. T. Tolley, "Design, fabrication and control of origami robots," *Nat. Rev. Mater.*, vol. 3, pp. 101–112, Jun. 2018.

[6] S. Felton, M. Tolley, E. Demaine, D. Rus, and R. Wood, "A method for building self-folding machines," *Science*, vol. 345, no. 6197, pp. 644–646, 2014.

[7] M. Schenk and S. D. Guest, "Geometry of miura-folded metamaterials," *Proc. Nat. Acad. Sci. USA*, vol. 110, no. 9, pp. 3276–3281, 2013.

[8] V. Srinivas and R. L. Harne, "Directing acoustic energy by flasher-based origami inspired arrays," *J. Acoust. Soc. America*, vol. 148, pp. 2935–2944, Nov. 2020.

[9] V. Srinivas and R. L. Harne, "Acoustic wave focusing by doubly curved origami-inspired arrays," *J. Intell. Mater. Syst. Struct.*, vol. 31, pp. 1041–1052, May 2020.

[10] C. Zou and R. L. Harne, "Tailoring reflected and diffracted wave fields from tessellated acoustic arrays by origami folding," *Wave Motion*, vol. 89, pp. 193–206, Jun. 2019.

[11] R. L. Harne and D. T. Lynd, "Origami acoustics: Using principles of folding structural acoustics for simple and large focusing of sound energy," *Smart Mater. Struct.*, vol. 25, no. 8, 2016, Art. no. 085031.

[12] X. Liu, S. Yao, B. S. Cook, M. M. Tentzeris, and S. V. Georgakopoulos, "An origami reconfigurable axial-mode bifilar helical antenna," *IEEE Trans. Antennas Propag.*, vol. 63, no. 12, pp. 5897–5903, Dec. 2015.

[13] K. Fuchi, J. Tang, B. Crowgey, A. R. Diaz, E. J. Rothwell, and R. O. Ouedraogo, "Origami tunable frequency selective surfaces," *IEEE Antennas Wireless Propag. Lett.*, vol. 11, pp. 473–475, 2012.

[14] K. Fuchi, A. R. Diaz, E. J. Rothwell, R. O. Ouedraogo, and J. Tang, "An origami tunable metamaterial," *J. Appl. Phys.*, vol. 111, no. 8, 2012, Art. no. 084905.

[15] D. Sessions, A. Cook, K. Fuchi, A. Gillman, G. Huff, and P. Buskohl, "Origami-inspired frequency selective surface with fixed frequency response under folding," *Sensors*, vol. 19, no. 21, p. 4808, Nov. 2019.

[16] Y. Cui, S. A. Nauroze, and M. M. Tentzeris, "Novel 3D-printed reconfigurable origami frequency selective surfaces with flexible inkjet-printed conductor traces," in *IEEE MTT-S Int. Microw. Symp. Dig.*, Jun. 2019, pp. 1367–1370.

[17] S. A. Nauroze, L. S. Novelino, M. M. Tentzeris, and G. H. Paulino, "Continuous-range tunable multilayer frequency-selective surfaces using origami and inkjet printing," *Proc. Nat. Acad. Sci. USA*, vol. 115, pp. 13210–13215, Dec. 2018.

[18] S. Alharbi *et al.*, "E-textile origami dipole antennas with graded embroidery for adaptive RF performance," *IEEE Antennas Wireless Propag. Lett.*, vol. 17, pp. 2218–2222, Dec. 2018.

[19] R. J. Lang. (1998). *Treemaker 4.0: A Program for Origami Design*. [Online]. Available: http://www.langorigami.com/article/treemaker

[20] T. Tachi, "Simulation of rigid origami," *Origami*, vol. 4, pp. 175–187, Jan. 2009.

[21] E. A. P. Hernandez, D. J. Hartl, E. Akleman, and D. C. Lagoudas, "Modeling and analysis of origami structures with smooth folds," *Comput.-Aided Design*, vol. 78, pp. 93–106, Sep. 2016. [Online]. Available: http://www.sciencedirect.com/science/article/pii/S0010448516300306

[22] Y. Kase, Y. Kanamori, and J. Mitani, "A method for designing flat-foldable 3D polygonal models," in *Proc. Int. Design Eng. Techn. Conf. Comput. Inf. Eng. Conf. (ASME)*, 2015, Art. no. V05BT08A034.

[23] F. Feng, X. Dang, R. D. James, and P. Plucinsky, "The designs and deformations of rigidly and flat-foldable quadrilateral mesh origami," *J. Mech. Phys. Solids*, vol. 142, Sep. 2020, Art. no. 104018.

[24] K. Abdul-Sater, "A hexagonal prism folding for membrane packaging based on concepts of finite rigid motion and kinematic synthesis," in *Proc. Int. Design Eng. Tech. Conf. Comput. Inf. Eng. Conf. (ASME)*, 2016, Art. no. V05BT07A004.

[25] X. Dang, F. Feng, P. Plucinsky, R. D. James, H. Duan, and J. Wang. (Aug. 2020). *Inverse Design of Deployable Origami Structures That Approximate a General Surface*. [Online]. Available: http://arxiv.org/abs/2008.02349.

[26] K. Fuchi *et al.*, "Spatial tuning of a RF frequency selective surface through origami," in *Proc. SPIE Defense Security*, 2016, pp. 1–10.

[27] D. Sessions *et al.*, "Investigation of fold-dependent behavior in an origami-inspired FSS under normal incidence," *Progr. Electromagn. Res. M*, vol. 63, pp. 131–139, Jan. 2018.

[28] K. Fuchi, G. Bazzan, A. S. Gillman, G. H. Huff, P. R. Buskohl, and E. J. Alyanak, "Frequency tuning through physical reconfiguration of a corrugated origami frequency selective surface," in *Proc. IEEE Int. Symp. Antennas Propag. USNC/URSI Nat. Radio Sci. Meeting*, Jul. 2017, pp. 411–412.

[29] Y. Cui, R. Bahr, S. V. Rijs, and M. Tentzeris, "A novel 4-DoF wide-range tunable frequency selective surface using an origami 'eggbox' structure," *Int. J. Microw. Wireless Technol.*, vol. 13, no. 7, pp. 1–7, May 2021.

[30] S. Yao, S. V. Georgakopoulos, B. Cook, and M. Tentzeris, "A novel reconfigurable origami accordion antenna," in *Proc. EEE/RSJ Int. Conf. Intell. Robots Syst.*, Chicago, IL, USA, 2014, pp. 14–18.

[31] S. Yao, X. Liu, J. Gibson, and S. V. Georgakopoulos, "Deployable origami yagi loop antenna," in *Proc. IEEE Int. Symp. Antennas Propag. USNC/URSI Nat. Radio Sci. Meeting*, 2015, pp. 2215–2216.

[32] S. I. H. Shah, M. M. Tentzeris, and S. Lim, "Low-cost circularly polarized origami antenna," *IEEE Antennas Wireless Propag. Lett.*, vol. 16, pp. 2026–2029, 2017.

[33] G. J. Hayes, Y. Liu, J. Genzer, G. Lazzi, and M. D. Dickey, "Self-folding origami microstrip antennas," *IEEE Trans. Antennas Propag.*, vol. 62, no. 10, pp. 5416–5419, Oct. 2014.

[34] G. H. Huff *et al.*, "A physically reconfigurable structurally embedded vascular antenna," *IEEE Trans. Antennas Propag.*, vol. 65, no. 5, pp. 2282–2288, May 2017.

[35] B. L. Cumby, G. J. Hayes, M. D. Dickey, R. S. Justice, C. E. Tabor, and J. C. Heikenfeld, "Reconfigurable liquid metal circuits by laplace pressure shaping," *Appl. Phys. Lett.*, vol. 101, no. 17, 2012, Art. no. 174102. [Online]. Available: https://doi.org/10.1063/1.4764020

[36] B. A. Munk, *Frequency Selective Surfaces: Theory and Design*. New York, NY, USA: Wiley, 2005.

[37] A. Gillman, K. Fuchi, and P. R. Buskohl, "Truss-based nonlinear mechanical analysis for origami structures exhibiting bifurcations and limit point instabilities," *Int. J. Solids Struct.*, vol. 147, no. 15, pp. 80–93, 2018.

[38] J. D. Baena *et al.*, "Equivalent-circuit models for split-ring resonators and complementary split-ring resonators coupled to planar transmission lines," *IEEE Trans. Microw. Theory Techn.*, vol. 53, no. 4, pp. 1451–1461, Apr. 2005.

[39] D. Rolando, "A lattice-based equivalent circuit model for frequency selective surfaces," M.S. thesis, Elect. Eng., Texas A&M Univ., College Station, TX, USA, 2014.

[40] T. Nomura, K. Sato, K. Taguchi, T. Kashiwa, and S. Nishiwaki, "Structural topology optimization for the design of broadband dielectric resonator antennas using the finite difference time domain technique," *Int. J. Numer. Methods Eng.*, vol. 71, no. 11, pp. 1261–1296, 2007.

[41] N. Aage and B. S. Lazarov, "Parallel framework for topology optimization using the method of moving asymptotes," *Struct. Multidiscipl. Optim.*, vol. 47, no. 4, pp. 493–505, Apr. 2013. [Online]. Available: https://doi.org/10.1007/s00158-012-0869-2

[42] S. D. Campbell, Y. Wu, E. B. Whitting, L. Kang, P. L. Werner, and D. H. Werner, "Synthesizing high-performance reconfigurable meta-devices through multi-objective optimization," in *Proc. Int. Appl. Comput. Electromagn. Soc. Symp.*, 2020, pp. 1–2.

[43] J. Xu *et al.*, "Multi-objective optimization of directivity-enhancing grin lenses," in *Proc. IEEE Int. Symp. Antennas Propag. North Amer. Radio Sci. Meeting (IEEECONF)*, Jul. 2020, pp. 1977–1978.

[44] M. Schenk and S. D. Guest, "Origami folding: A structural engineering approach," in *Proc. Origami*, 2011, pp. 291–304.

[45] K. Liu and G. Paulino, "Nonlinear mechanics of non-rigid origami: An efficient computational approach," *Proc. Roy. Soc. A*, vol. 473, no. 2206, 2017, Art. no. 20170348.

[46] J.-M. Jin, *The Finite Element Method in Electromagnetics*, 2nd ed. New York, NY, USA: Wiley, 2002.

[47] J.-M. Jin and D. J. Riley, *Finite Element Analysis of Antennas and Arrays*, 1st ed. Hoboken, NJ, USA: Wiley, 2009.

[48] K. Svanberg, "The method of moving asymptotes—A new method for structural optimization," *Int. J. Numer. Methods Eng.*, vol. 24, no. 2, pp. 359–373, 1987.

[49] J. S. Jakob, "Topology optimization of dynamics problems with Padé approximants," *Int. J. Numer. Methods Eng.*, vol. 72, no. 13, pp. 1605–1630, 2007. [Online]. Available: https://onlinelibrary.wiley.com/doi/abs/10.1002/nme.2065

[50] T. Nomura, S. Nishiwaki, K. Sato, and K. Hirayama, "Topology optimization for the design of periodic microstructures composed of electromagnetic materials," *Finite Elements Anal. Design*, vol. 45, no. 3, pp. 210–226, 2009. [Online]. Available: http://www.sciencedirect.com/science/article/pii/S0168874X08001509

[51] N. Aage, O. Sigmund, and O. Breinbjerg, "Topology optimization of radio frequency and microwave structures," Ph.D. dissertation, Dept. Mech. Eng. Tech. Univ. Denmark, Kongens Lyngby, Denmark, 2011.

[52] K. Fuchi *et al.*, "Origami actuator design and networking through crease topology optimization," *J. Mech. Design*, vol. 137, no. 9, 2015, Art. no. 091401.

[53] A. Gillman, K. Fuchi, G. Bazzan, E. J. Alyanak, and P. R. Buskohl, "Discovering origami fold patterns with optimal actuation through nonlinear mechanics analysis," in *Proc. Int. Design Eng. Tech. Conf. Comput. Inf. Eng. Conf. (ASME)*, 2017, Art. no. V05BT08A052.

[54] M. P. Bendsøe and O. Sigmund, "Material interpolation schemes in topology optimization," *Archive Appl. Mech.*, vol. 69, no. 9, pp. 635–654, 1999. [Online]. Available: https://doi.org/10.1007/s004190050248

[55] L. Van Der Maaten and G. Hinton, "Visualizing data using t-SNE," *J. Mach. Learn. Res.*, vol. 9, pp. 2579–2605, Nov. 2008.